The current issue and full text archive of this journal is available at
www.emeraldinsight.com/0264-4401.htm

Fourier series based finite element analysis of tube hydroforming

An axisymmetric model

Yabo Guan
Department of Neurosurgery, Medical College of Wisconsin, Milwaukee, Wisconsin, USA

Farhang Pourboghrat
Mechanical Engineering Department, Michigan State University, East Lansing, Michigan, USA, and

Woong-Ryeol Yu
School of Materials Science and Engineering, Seoul National University, Seoul, Korea

Abstract

Purpose – The purpose of this paper is to provide an axisymmetric model of tube hydroforming using a Fourier Series based finite element method.

Design/methodology/approach – Fourier series interpolation function, which considerably reduces the size of the global stiffness matrix and the number of variables, is employed to approximate displacements. The material of the tube is assumed to be elastic-plastic and to satisfy the plasticity model that takes into account the rate independent work hardening and normal anisotropy. Numerical solution obtained from an updated Lagrangian formulation of the general shell theory is employed. The axial displacement stroke (a.k.a. axial feed) during tube hydroforming is incorporated using Lagrange multipliers. Contact constraints and boundary friction condition are introduced into the formulation based on the penalty function, which imposes the constraints directly into the tangent stiffness matrix. A forming limit curve based on shear instability and experimental measurements are used as fracture criteria.

Findings – The results obtained from this new formulation are compared against the nonlinear finite element code ABAQUS and experimental measurements for isotropic and transversely anisotropic tube materials. The hoop and axial strains predicted with AXHD code compared excellently with those from ABAQUS FEM code using plane stress axisymmetric (SAX1) and four-node shell (S4R) elements. However, in the case of aluminum, the numerically predicted maximum hoop strain underestimated the actual hoop strain measured from the tube bulging experiment.

Practical implications – The axisymmetric hydroforming program (AXHD) developed in this work is very efficient in simulating the free-forming stage of the tube hydroforming process under simultaneous action of internal pressurization and displacement stroke.

The authors wish to acknowledge with thanks the National Science Foundation for the support of this project through the grant DMI 0084992 in conjunction with Alcoa through the GOALI program. The authors would also like to express their gratitude to Prof. Edmundo Corona for his careful review of the manuscript.

Engineering Computations:
International Journal for
Computer-Aided Engineering and
Software
Vol. 23 No. 7, 2006
pp. 697-728

0264-4401
DOI 10.1108/02644400610689866

Originality/value – Although Fourier Series based finite element method has been used in metal forming, the extended application presented in this paper is novel in the finite element analysis of tube hydroforming.

Keywords Steel, Finite element analysis, Metals, Fourier transforms, Material-removal processes

Paper type Research paper

Nomenclature

$\underline{D}$ = strain rate tensor
$\underline{L}$ = fourth-order elastic tensor
E = Young's modulus
h = plastic hardening parameter
n = strain hardening exponent
R = normal anisotropy parameter
t = thickness of the shell
u, w = incremental displacements of the mid-surface of the shell
λ_1, λ_2 = principal stretches of the shell
$\underset{\sim}{\sigma}^{\nabla}$ = Jaumann rate of stress tensor
$\dot{\underset{\sim}{\sigma}}$ = material time derivative of stress tensor
$\underline{\sigma}$ = stress tensor
$\bar{\sigma}$ = effective stress
$\bar{\varepsilon}$ = effective strain
τ = time
ν = Poisson ratio
σ_y = initial yield strength of material
ε_r = circumference strain for straight segment
ε_r^0 = membrane component of circumference strain for straight segment
σ_r = circumference stress for straight segment
κ_r = first principal curvature of the tube
ε_s = axial strain for straight segment
ε_s^0 = membrane component of axial strain for straight segment
σ_s = axial stress for straight segment
κ_s = second principal curvature of the tube
p = internal pressure
T = tension
λ = Lagrange multipliers
$\hat{n}$ = unit outward normal to the mid-surface of shell
u^* = displacement stroke
τ_i = frictional traction force
r^i = current radius of the deformed tube
α = stress ratio
ρ = strain ratio
β = $1 + R^{1/(1-a)}$
a = order of Yield function (= 2)
ε_1^* = maximum principal strain at shear instability
ε_{1p}^* = maximum principal strain from plane strain test
( ), = indicates derivative with respect to a parameter

1. Introduction

Hydroforming offers a way to cut material and manufacturing costs while improving product performance in a variety of applications. Advantages include weight reduction due to improved part design, part consolidation where a single component replaces an assembly, reduced tooling cost as a result of part consolidation, and improved structural strength and stiffness of the hydroformed component. Thus, it reduces tooling, part, and labor costs, while significantly improving product performance (Anon, 1997).

While numerous variations of hydroforming exist, the basic principle remains the same: utilize fluid pressure to form a component. Both traditional high-pressure hydroforming and pressure sequence hydroforming are presented in Longhouse (1998) and Morphy (1997). Typical Hydroforming sequence is shown in Figure 1, where internal pressure and axial feed (force or displacement) are applied simultaneously to improve the material shaping abilities. The process is being used to make a wide range of complex cylindrical, flat and tubular components. Cylindrical parts include gas

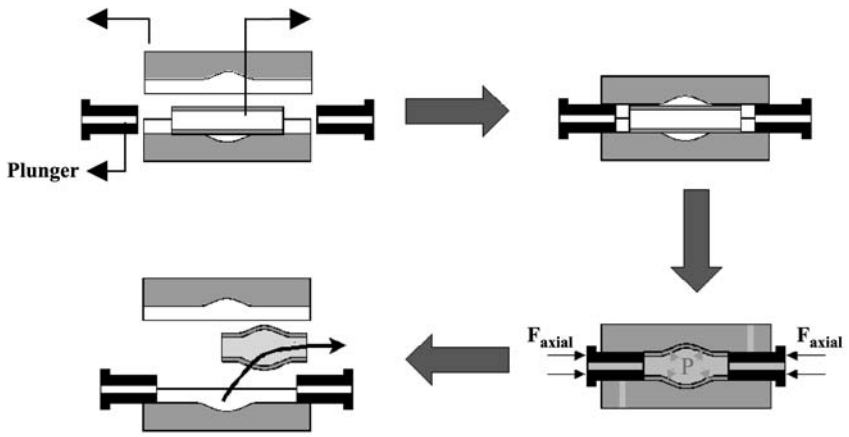

Figure 1.
Force-controlled hydroforming process derived from: siempelkamp pressen systeme GmbH & Co

cylinders, washing-machine drums and cooker cavities. Flat components include auto body panels, fuel tanks and aerospace parts.

Built on the successful application of finite element method to metal forming processes (Wang and Budiansky, 1978; Oh, 1982; Nagteggal and Rebelo, 1988; Wang and Tang, 1988; Kobayashi *et al.*, 1989), explicit finite element method has been used for the simulation of stamping and hydroforming process by Ni (1994) and to bulging of sheet metals by Hu *et al.* (1997). Hsu and Chu (1995) applied explicit finite element method to a sheet metal operation involving punch stretching, drawing and hydroforming. Berg and Hora (1996) developed a specific hybrid shell to simulate the hydroforming of sheet and tubular structures using an explicit formulation. Noh and Yang (1998) derived an upper bound solution for the hydroforming of arbitrarily shaped boxes from blank sheets.

Using the explicit finite element code LS-Dyna3D, Srinivasan *et al.* (1998) provided additional correlation of experimental and simulation results for tube hydroforming, and Liu *et al.* (1998) provided analytical and experimental examination of tube hydroforming limits. Kaya *et al.* (2002) performed plane strain analysis of crushing and expansions of tube cross-sections using the two-dimensional implicit finite element code DEFORM 2D. Kim *et al.* (2002) developed a rigid-plastic finite element method for the analysis of tube hydroforming process. Other numerical analyses of tube hydroforming performed recently can be found in Papelnjak (2004), Hama *et al.* (2003, 2004a, b), Lin and Kwan (2004), Hwang and Altan (2003, 2004) and Lang *et al.*, 2004).

Selection of load (internal pressure) and end condition (axial feed) will affect the formability of a metallic tube in the tube hydroforming process. The influence of these parameters was studied by Imaninejad *et al.* (2004), Ray and MacDonald (2004), Aue-U-Lan *et al.* (2004), Johnson *et al.* (2004), Hsu (2003) and Fann and Hsiao (2003).

Most recently, researchers studied failure phenomenon (wrinkling, bursting, necking, etc.) due to local instability during tube hydroforming. Prediction of failure initiation using finite element method and applying stability criteria was investigated by Aydemir *et al.* (2005), Kulkarni *et al.* (2004), Kim and Kang (2004) and Kim *et al.* (2003, 2004).

Miller *et al.* (2001a) experimentally investigated the bend-stretch-pressure forming of aluminum extruded-tubes and found that tension and modest levels of pressurization prevents buckling of the compressed side, reduces springback and distortion of the bent tube. In support of these experiments, Miller *et al.* (2001b) developed a CPU-efficient 2D model for the bend-stretch-pressure forming process, which assumes that the tube shape and all applied loads are uniform along its length. Owing to its computational efficiency, they were able to design the process and to evaluate some possible alternative loading histories, which would result in minimum distortion and springback of the cross section of the tube after the bending. Corona (2004) extended the sectional analysis to accommodate more general cross-sections.

In this paper an axisymmetric analysis method is presented for calculating strains and expansion as the tube is subjected to simultaneous internal pressure and axial displacement stroke, a.k.a. axial feed. The present method employs some simplifying assumptions. The principal geometrical assumption is that the representative meridian of the tube is initially straight. This assumption however could be relaxed by using a curved, instead of a straight segment to represent the initial geometry of the tube. All segments making up the meridian are assumed to be relatively thin and of constant thickness. The deformation of the tube is assumed not to vary along its cross-section, hence, the analysis could be considered to be an axisymmetric analysis.

The Fourier series based implicit Axisymmetric Hydroforming (AXHD) program is an extension of the work by Miller *et al.* (2001b) and Corona (2004). The material of the tube is assumed to be elastic-plastic and to satisfy the plasticity model that takes into account rate-independent work hardening and normal anisotropy (Pourboghrat *et al.*, 2000). Frictional stress at the die-tube interface is assumed to be proportional to the contact pressure based on Coulomb friction model. By using the virtual work principle and constitutive equation, the equilibrium equation can be derived. Numerical solution obtained from an updated-Lagrangian formulation of a general shell theory is employed. Axial stroke is incorporated into the equilibrium equation using Lagrange Multiplier technique. The boundary friction condition is introduced into the formulation in the form of a penalty function, which imposes the constraint directly into the tangent stiffness matrix. The Newton-Raphson algorithm is used to solve the nonlinear equations.

If hydroforming technology is to be applied economically, it is essential to have knowledge of the avoidance of failure cases as well as of the behavior of the tube in the tool under the compressive stress and forces that are exerted by the machine (i.e. axial feed). Several failure modes, buckling, wrinkling and bursting are discussed in Dohmann and Hartl (1996) and Asnafi (1999). To that end, forming limit curve (FLC) developed based on the onset of shear instability (Lee and Kim, 1989) and experimental measurements are incorporated into AXHD code as fracture criteria.

In Section 2 of this paper the thin shell model is described. The kinematics assumptions and principal strain formulations are discussed in Section 3. The constitutive model and contact algorithm are described in Sections 4 and 5, respectively. Section 6 describes the equilibrium equation formulations based on the virtual work principle (VWP) and the application of Newton-Raphson iterative method to solve the resulting non-linear equations. The flowchart of AXHD program and fracture criteria is detailed in Sections 7 and 8, respectively. Finally, in Section 9 several examples are provided in support of the section-analysis finite element model, where

numerical predictions of the deformed shape, hydroforming pressure, and deformation strains are compared with experimental measurements and the nonlinear finite element code ABAQUS.

2. Thin shell theory

Pourboghrat *et al.* (2000) derived the principal curvatures and stretches of a shell of revolution undergoing axisymmetric deformation using both total and updated Lagrangian formulations. For completeness, the basic formulation for updated Lagrangian theory will be discussed next.

The deformation of the mid-surface of an element will be considered based on thin shell theory. Figure 2 shows the shell mid-surface at the reference time ${}^{o}t$ and the current time t as it bends and stretches.

2.1 Principal curvature and stretch (updated Lagrangian)

After bending and stretching, the principal mid-surface curvature, k_1, of a shell element at the current configuration, t $(= {}^{o}t + \Delta t)$, could be calculated from the known information about the element at the reference configuration (time ${}^{o}t$, see Figure 2), as follows:

$$\underset{\sim}{r} = \underset{\sim}{R} + u\hat{\underset{\sim}{A}} + w\hat{\underset{\sim}{N}} \tag{1}$$

where $\underset{\sim}{R}$ is the reference configuration at time ${}^{o}t$ and u and w are incremental displacements defined in Figure 2. In equation (1), the unit tangent vector $\hat{\underset{\sim}{A}}$ and the unit principal normal vector $\hat{\underset{\sim}{N}}$ to the mid-surface of the reference configuration are defined as:

$$\hat{\underset{\sim}{A}} = \frac{\partial \underset{\sim}{R}}{\partial S} = \underset{\sim}{R}_{,s} \tag{2}$$

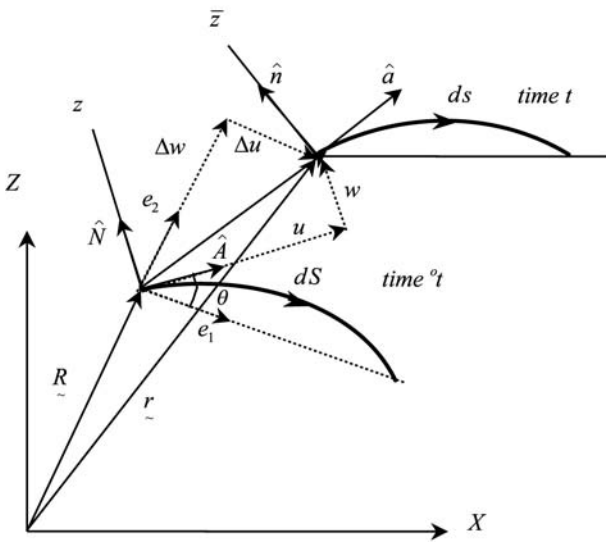

Figure 2.
Shell mid-surface at reference time ${}^{o}t$ and current time t

$$\hat{\underline{N}} = \frac{\hat{\underline{A}}_{,s}}{K_1} \quad \text{or,} \quad \hat{\underline{A}} = -\frac{\hat{\underline{N}}_{,s}}{K_1} \tag{3}$$

where K_1 is the centerline curvature at the reference configuration. To calculate the centerline curvature at current configuration, k_1, the unit tangent vector $\hat{\underline{a}}(= \underline{a}/\|\underline{a}\|)$ and the unit principal normal vector of the mid-surface of the shell $\hat{\underline{n}}(= \underline{n}/\|\underline{n}\|)$ must be known. Using equation (1), the tangent vector $\underline{a}$ is calculated as:

$$\underline{a} = \frac{\partial \underline{r}}{\partial S} = \underline{r}_{,s} = \underline{R}_{,s} + u_{,s}\hat{\underline{A}} + u\hat{\underline{A}}_{,s} + w_{,s}\hat{\underline{N}} + w\hat{\underline{N}}_{,s} \tag{4}$$

After substituting from equations (2) and (3) into equation (4), and some re-arranging, the following expression results:

$$\underline{a} = \frac{\partial \underline{r}}{\partial S} = \underline{r}_{,s} = (1 + u_{,s} - K_1 w)\hat{\underline{A}} + (w_{,s} + K_1 u)\hat{\underline{N}} = c\hat{\underline{A}} + d\hat{\underline{N}} \tag{5}$$

The principal incremental stretch of the mid-surface in the axial direction calculated from the magnitude of the base vector $\underline{a}$ in equation (5) is:

$$\lambda_1 = \|\underline{a}\| = \sqrt{\underline{a}\cdot\underline{a}} = \sqrt{c^2 + d^2} = [(1 + u_{,S} - K_1 w)^2 + (w_{,S} + K_1 u)^2]^{1/2} \tag{6}$$

The current length of the mid-surface of the shell in the axial direction, ds, is calculated from the reference length, dS, and λ_1 as follows:

$$ds = \lambda_1 dS \tag{7}$$

The unit principal normal vector of the surface of the current shell, $\hat{\underline{n}}$, is:

$$\hat{\underline{n}} = \frac{-d\hat{\underline{A}} + c\hat{\underline{N}}}{\lambda_1} \tag{8}$$

which from equations (5), (6) and (8), shows that $\hat{\underline{n}}\cdot\hat{\underline{a}} = 0$. The current principal curvature of the shell, k_1, could now be found as:

$$k_1 = -\hat{\underline{a}}\cdot\hat{\underline{n}}_{,s} = -\underline{r}_{,s}\cdot\hat{\underline{n}}_{,s} = -\frac{1}{\lambda_1^2}\underline{a}\cdot\hat{\underline{n}}_{,S} \tag{9}$$

where $\underline{a}$ is given by equation (4) and $\hat{\underline{n}}_{,s}$ can be derived from equation (8) as:

$$\hat{\underline{n}}_{,S} = \frac{d\hat{\underline{n}}}{dS} = \frac{\lambda_1\cdot(d_{,S}\hat{\underline{A}} + c_{,S}\hat{\underline{N}} - K_1 c\hat{\underline{A}} - K_1 d\hat{\underline{N}}) - \lambda_{1,S}\cdot(-d\hat{\underline{A}} + c\hat{\underline{N}})}{\lambda_1^2} \tag{10}$$

In equation (10), $\lambda_{1,S}$ is assumed to vanish within an element and the above expression simplifies as:

$$\hat{\underline{n}}_{,S} = -\frac{(d_{,S} + K_1 c)\hat{\underline{A}} + (-c_{,S} + K_1 d)\hat{\underline{N}}}{\lambda_1} \tag{11}$$

After substituting from equations (5), (6) and (11) into equation (9), the current centerline curvature of the shell, k_1, can be found:

$$k_1 = \frac{cd_{,S} - dc_{,S} + K_1\lambda_1^2}{\lambda_1^3} \tag{12}$$

3. Kinematics of the straight segment

Using the updated Lagrangian formulation, exact expressions for membrane strains, normal vector rotation, and principal curvatures of an axisymmetric shell element were derived in Section 2 (Shell element model). By using in these expressions the values of displacements and curvatures of the shell at previous time increment (i.e. $t = {}^{o}t$), one would recover the *incremental* values of strains. However, by using in these expressions the values of displacements and curvatures of the shell at the initial time (i.e. $t = 0$) one would recover the total values of strains. In this paper, the difference between the total strains at time t (current) and ${}^{o}t$ (previous) is used to calculate the incremental strains, i.e. $\Delta\varepsilon = \varepsilon(Y, t) - \varepsilon(Y, {}^{o}t)$, where Y corresponds to the location of a material point on the meridian of the tube.

In the Appendix, based on the kinematics of the mid-surface of the shell (Section 2), a set of kinematics equations is derived suitable for solving the tube bulging problem using a number of small deformation increments. The underlying assumption used in these derivations is that the accumulated error associated with dropping the quadratic term in the definition of total strain is negligible. The table in the Appendix shows the magnitude of the error associated with this assumption.

3.1 Kinematics assumptions

For the purpose of modeling, all segments making up the meridian are assumed to be thin and of constant thickness. To meet the thin shell assumption, the length of the straight segments should be greater than ten times the thickness. The deformation of the structural member is assumed not to vary along its cross-section for a given point on the meridian. Hence, the analysis can be done for a straight meridian parallel to the axis of the tube, as shown in Figure 3. Nonlinear expressions for incremental deformation (i.e. strain, displacement, rotation) and curvature will be derived for the straight segment as functions of nodal displacements (u, w), and their derivatives ($u_{,S}, u_{,SS}, w_{,S}, w_{,SS}$). Details of these derivations are shown in the Appendix.

3.2 Principal strains

The representative meridian shown in Figure 3 lies in the plane defined by the Y- and Z-axes. In this formulation, the initial geometry of the tube is represented with a pair of

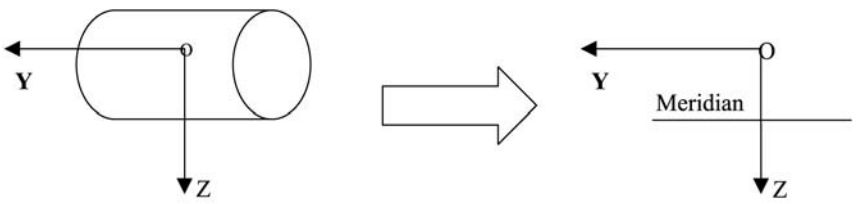

Figure 3.
Representative meridian for axisymmetric case

Y-Z coordinates defining the meridian line. The meridian is then subdivided into a number of straight shell segments, with each segment defined using two nodes.

The kinematics, strains and curvature expressions for a straight shell segment under axisymmetric loading are defined here. For the straight segment shown in Figure 4 the local coordinates of the segment are s along the segment and z in the through-thickness direction. The initial segment geometry is defined by the location of the point $s = 0$ given by Y_0 and Z_0, the orientation angle θ the length l_o and the thickness t of the segment. The position $z = 0$ is located at the mid-surface of the straight segment, indicated by the dashed line. The displacement components of the mid-surface are u and w along the original s and z directions, respectively.

The angle of rotation β between the current normal vector $\hat{n}$ and the original normal vector $\hat{N}$ could be approximated as (see Appendix):

$$\sin\beta \approx \beta = -\frac{w_{,S}}{\sqrt{1+w_{,S}^2}} \tag{13}$$

The validity of equation (13) will be tested by comparing the deformed shape as well as predicted hoop and axial strains of a bulged tube with similar results obtained with ABAQUS using the nonlinear axisymmetric (SAX1) and shell elements (S4R).

The total axial strain ε_s through-the-thickness of the tube is given by:

$$\varepsilon_s = \varepsilon_s^0 + \kappa_s z \tag{14}$$

where ε_s^0 is the axial strain of the mid-surface of the shell given by (see Appendix):

$$\varepsilon_s^0 = u_{,S} + \frac{1}{2}\left(u_{,S}^2 + w_{,S}^2\right) \tag{15}$$

and the local curvature κ_s due to bending of the shell about the X-axis, is given by:

$$\kappa_s = \frac{w_{,SS}}{\left(1+w_{,S}^2\right)^{3/2}} \tag{16}$$

The total strain in the circumferential (hoop) direction is given by:

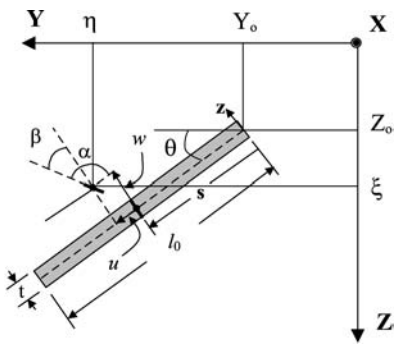

Figure 4.
The general description of the geometry of a straight segment

$$\varepsilon_r = \varepsilon_r^0 + \kappa_r z \tag{17}$$

where ε_r^0 is the hoop strain at a point on the mid-surface, which can be found from the change in the radius of the tube as:

$$\varepsilon_r^0 = \frac{\xi - (Z_0 + s\sin\theta - z\cos\theta)}{r} = \frac{u\sin\theta - w\cos\theta + z\beta\sin\theta}{r} \tag{18}$$

where r is the original radius of the tube, and the local curvature κ_r, due to bending about the Y-axis, is given by:

$$\kappa_r = -\frac{1}{r}\frac{\partial w}{\partial S} = -\frac{w_{,S}}{r} \tag{19}$$

3.3 Constraints

Since, the meridian of the tube is comprised of several connected straight segments, with their own local coordinate systems and variables, it is necessary to enforce compatibility of deformations at junctions of two neighboring segments. The coordinates of a point on a segment undergoing displacements u and w from the original configuration are (Figure 4):

$$\xi = Z_0 + (s+u)\sin\theta - w\cos\theta + z(-\cos\theta + \beta\sin\theta) \tag{20a}$$

$$\eta = Y_0 + (s+u)\cos\theta + w\sin\theta + z(\sin\theta + \beta\cos\theta) \tag{20b}$$

Based on equations (20a) and (20b), the following three constraint equations could be written to ensure compatibility of displacements and rotations between two neighboring segments:

$$u_2\cos\theta_2 + w_2\sin\theta_2 - u_1\cos\theta_1 - w_1\sin\theta_1 = 0 \tag{21}$$

$$u_2\sin\theta_2 - w_2\cos\theta_2 - u_1\sin\theta_1 + w_1\cos\theta_1 = 0 \tag{22}$$

$$\beta_2 - \beta_1 = 0 \tag{23}$$

4. Constitutive equation

The elastic-plastic, rate-independent constitutive model implemented in the axisymmetric formulation of tube hydroforming analysis code assumes isotropic hardening and is based on Pourboghrat *et al.* (2000). The uniaxial stress-plastic strain curve of the material is assumed to have the following power-law form:

$$\bar{\sigma} = K(\bar{\varepsilon} + \bar{\varepsilon}_o)^n \tag{24}$$

where $\bar{\sigma}$ is the effective stress and $\bar{\varepsilon}$ is the effective plastic strain. Parameters K, n and $\bar{\varepsilon}_0$ are material constants that are calculated by curve fitting equation (24) to an actual stress-strain data measured from a uniaxial tensile test. The elastic strain increment is related to the stress increment through the equations of linear isotropic elasticity with Young's modulus E and Poisson's ratio ν. The yield function given below allows for anisotropic yielding of the material:

$$\phi = \frac{\sigma_s^2 + \sigma_r^2 + R(\sigma_s - \sigma_r)^2}{1+R} - \bar{\sigma}^2 = 0 \tag{25}$$

where R is the normal anisotropy parameter.

During the loading, Hooke's law is employed to calculate stress below the elastic limit;, i.e. $\bar{\sigma} \leq \sigma_y$, where σ_y is the initial yield stress of the tube material obtained from a uniaxial tensile test. Beyond the elastic limit;, i.e. $\bar{\sigma} > \sigma_y$, the co-rotational time derivative of stress (Jaumann stress rate) is calculated, for a given strain rate, from an elastic-plastic constitutive equation:

$$\overset{\nabla}{\underset{\sim}{\sigma}} = \left[\underset{\sim}{L} - \frac{\underset{\sim}{L} : \underset{\sim}{P}\underset{\sim}{P} : \underset{\sim}{L}}{h\frac{\underset{\sim}{P}:\sigma}{\bar{\sigma}} + \underset{\sim}{P} : \underset{\sim}{L} : \underset{\sim}{P}} \right] : \underset{\sim}{D} \tag{26}$$

Here $\overset{\nabla}{\underset{\sim}{\sigma}}$ and $\underset{\sim}{D}(= \underset{\sim}{D}^e + \underset{\sim}{D}^p)$ are the Jaumann rate of stress and strain rate tensors, respectively, $\underset{\sim}{\sigma}$ is the stress tensor, $h(= \partial\bar{\sigma}/\partial\bar{\varepsilon})$ is the plastic hardening parameter, $\underset{\sim}{L}$ is the fourth-order elastic tensor and $\underset{\sim}{P}(= (\partial\phi/\partial\underset{\sim}{\sigma})/\|\partial\phi/\partial\underset{\sim}{\sigma}\|)$, where $\|\partial\phi/\partial\underset{\sim}{\sigma}\| = \sqrt{\partial\phi/\partial\underset{\sim}{\sigma} : \partial\phi/\partial\underset{\sim}{\sigma}}$, is the second order tensor representing the unit normal to the flow potential. The effective plastic strain rate, associated with equation (26), is calculated from the following expression:

$$\dot{\bar{\varepsilon}} = \frac{\underset{\sim}{P} : \underset{\sim}{L} : \underset{\sim}{P} - \underset{\sim}{P} : \overset{\nabla}{\underset{\sim}{\sigma}}}{\frac{\bar{\sigma}}{\underset{\sim}{P}:\underset{\sim}{\sigma}}\underset{\sim}{P} : \underset{\sim}{L} : \underset{\sim}{P}} \tag{27}$$

The fourth-order elastic tensor $\underset{\sim}{L}(= L_{ijkl})$ used in this work is the standard tensor for the isotropic elasticity, which has only two independent components.

5. Contact algorithm

The tube hydroforming simulation requires modeling the frictional contact between the tube and the die. The contact analysis is complex because it requires accurate tracking of the motion of multiple bodies, and the motion due to the interaction of these bodies after the contact. The numerical objectives are to detect the motion of the bodies, apply a constraint to avoid penetration, and finally apply appropriate boundary conditions to simulate the frictional contact behavior. Each of these objectives will be separately described next.

5.1 Contact detection

To detect contact between the tube and the die, evenly spaced contact nodes are initially defined along the tube cross section (e.g. at $s_0, s_1 = s_0 + \Delta s$, etc.). During the contact analysis, the displacement of each contact node is checked for surface penetration, by determining whether it has crossed into the die. For this purpose, the calculation of the tube surface normal is required, since it is used to determine which segment on the die is closest to a potential contact node on the tube cross section. For example, as shown in Figure 5, the closest segment on the die (i.e. $\overline{B_{i-1}B_i}$ or $\overline{B_iB_{i+1}}$) to the contact node (A_k) on the tube can be determined using the following cross-product:

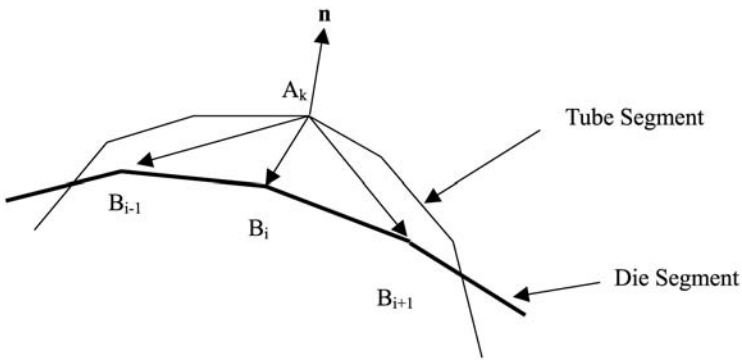

Figure 5.
Penetration of a contact node on the tube into the die

$$\text{If}: \quad \left(\vec{A_kB_i} \times \hat{n}\right) \cdot \left(\vec{A_kB_{i+1}} \times \hat{n}\right) < 0 \tag{28}$$

then, $\overline{B_iB_{i+1}}$ will be the die segment associated with the contact node A_k.

5.2 Projection algorithm

A nodal position produced by the trial solution may penetrate the die. By using the cross-product algorithm, the closest segment on the die corresponding to the contact node can be found. The nodal coordinates are then modified by a projection scheme such that the contact node just touches the die surface. As shown in Figure 6, PQ is assumed to be the die segment associated with the penetrated contact node A, point B is the intersection point between the normal vector and PQ, and O is the original location of the contact node. Based on the following vector equation, the coordinate of point B could be calculated:

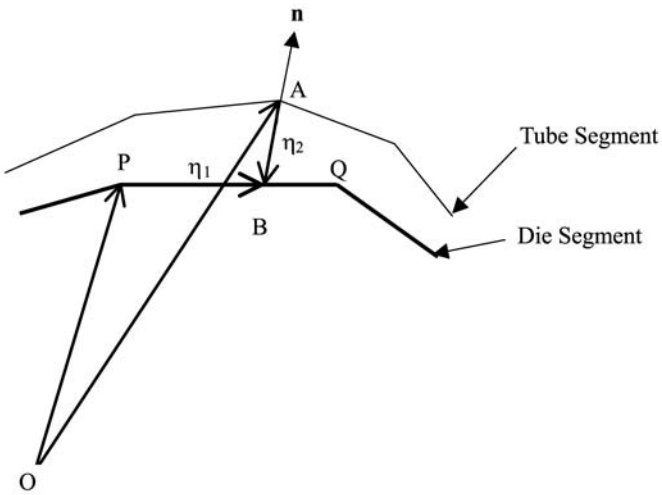

Figure 6.
The projection method for returning the contact node onto the die surface

$$\vec{OP} + \vec{PB} = \vec{OA} + \vec{AB} \tag{29a}$$

$$\vec{PB} = \eta_1 \frac{\vec{PQ}}{\|\vec{PQ}\|}, \vec{AB} = -\eta_2 \hat{n} \tag{29b}$$

where η_1, η_2 are scalar parameters. Once η_1, η_2 are solved for from equations (29a) and (29b), the coordinate of point B could be determined.

5.3 Implementation of contact constraints

A contact node projected onto the die surface at time $t + \Delta t$, is constrained to move in the tangent direction defined by the trial solution, $\Delta \underline{u}^*$. The constraint on the displacement vector $\delta \underline{u} = (\delta u, \delta w)$, for contacting nodes is then:

$$\delta \underline{u} \cdot \hat{n} = 0 \tag{30}$$

5.4 Separation of a node in contact

After a node on the tube comes into contact with the die surface, it is possible for it to separate in a subsequent iteration or deformation increment. Mathematically, a node should separate when the calculated reaction force between the contacting node on the tube and the die surface becomes tensile or positive.

When contact occurs, a reaction force associated with the contact node balances the internal stress of the element sharing this node. When separation occurs, this reaction force behaves as a residual force (as the force on a free node should be zero). This requires that the internal stresses in the deformable body be redistributed.

6. Equilibrium equation

The equilibrium equation is satisfied based on the virtual work principle. Unlike the traditional finite element method, nodal displacements in this formulation are approximated with Fourier series. The axial stroke is incorporated using Lagrange multipliers. Contact constraints and boundary friction condition (discussed in Section 5) are introduced into the formulation in the form of penalty functions, which imposes those constraints directly into the tangent stiffness matrix. The Newton-Raphson algorithm is used to iteratively solve the nonlinear equilibrium equations. The equilibrium equations associated with four types of loading commonly used in tube hydroforming, i.e. pressure loading, axial force, displacement stroke and frictional contact, will be described next.

6.1 Pressure loading model

Based on the kinematics and constitutive equations discussed in Sections 2-4, the principle of virtual work takes the following form for pressure loading:

$$\sum_{i=1}^{I} \int_{L^i} \left(\sigma_s^j \delta \varepsilon_s^i + \sigma_{r_i}^j \delta \varepsilon_{r_i}^i \right) r^i \mathrm{d}L^i + \sum_{j=1}^{J} \lambda_j \delta C_j = \delta W_{\mathrm{Ext}}^P \tag{31}$$

where I is total number of straight segments along the tube length (meridian), J is total number of constraint equations, λ_j are Lagrange multipliers, C_j are constraint

equations (21)-(23), $\delta W^{P}_{\text{Ext}}$ is the virtual work due to external force (pressure), $\mathrm{d}L^{i}$ is the incremental length for the straight segment, and r^{i} is the current radius of the segment. The total displacement components w^{i}, u^{i} for each straight segment, as measured from the original configuration, are approximated using the following Fourier series expressions:

$$w^{i} = \alpha_0^{i} + \sum_{n=1}^{N^{i}} \alpha_n^{i} \cos \frac{n\pi s_i}{l_i^0} + \sum_{n=1}^{N^{i}} \beta_n^{i} \sin \frac{n\pi s_i}{l_i^0} \tag{32a}$$

$$u^{i} = \gamma_0^{i} + \sum_{n=1}^{N^{i}} \gamma_n^{i} \cos \frac{n\pi s_i}{l_i^0} + \sum_{n=1}^{N^{i}} \delta_n^{i} \sin \frac{n\pi s_i}{l_i^0} \tag{32b}$$

where $\alpha_o, \alpha_n, \beta_n, \gamma_o, \gamma_n, \delta_n$ are the unknown series coefficients and s_i, l_i^0 represent the location of a point on the undeformed straight segment on the meridian and the original length of the straight segment,, respectively, (Figure 4). Then, Δw^{i} and Δu^{i} representing the incremental displacement components of a material point (Y) on the mid-surface, measured between times t (current) and ${}^{o}t$ (reference) (Figure 2), could be defined as:

$$\Delta w^{i} = w^{i}(Y,t) - w^{i}(Y,{}^{o}t) = \Delta\alpha_0^{i} + \sum_{n=1}^{N^{i}} \Delta\alpha_n^{i} \cos \frac{n\pi s_i}{l_i^0} + \sum_{n=1}^{N^{i}} \Delta\beta_n^{i} \sin \frac{n\pi s_i}{l_i^0} \tag{32c}$$

$$\Delta u^{i} = u^{i}(Y,t) - u^{i}(Y,{}^{o}t) = \Delta\gamma_0^{i} + \sum_{n=1}^{N^{i}} \Delta\gamma_n^{i} \cos \frac{n\pi s_i}{l_i^0} + \sum_{n=1}^{N^{i}} \Delta\delta_n^{i} \sin \frac{n\pi s_i}{l_i^0} \tag{32d}$$

where $\Delta\alpha_o, \Delta\alpha_n, \Delta\beta_n, \Delta\gamma_o, \Delta\gamma_n, \Delta\delta_n$ are unknown incremental changes in the series coefficients to be calculated. By substituting from equations (32a-b) or (32c-d) into the principle of virtual work, equation (31), a nonlinear expression of the following form will result:

$$f(\underset{\sim}{c}, P) = 0 \tag{33a}$$

where

$$\underset{\sim}{c} = \left\{\alpha_0^{i}, \alpha_n^{i}, \beta_n^{i}, \gamma_0^{i}, \gamma_n^{i}, \delta_n^{i}, \lambda_j\right\} \tag{33b}$$

Equation (33a) is then solved for the unknown vector $d\underset{\sim}{c}$ for given values of pressure P.

Since, equation (33a) is highly nonlinear, it will be iteratively solved by the Newton-Raphson method. The Newton-Raphson iterative method used to solve $d\underset{\sim}{c}$ will look like:

$$[\underset{\approx}{K}][d\underset{\sim}{c}] = \underset{\sim}{F}_{\text{Ext}} - \underset{\sim}{F}_{\text{Int}} \tag{34}$$

where $(\underset{\approx}{K}(= \partial^2 W_{\text{Int}}/\partial\underset{\sim}{c}\partial\underset{\sim}{c}))$ is the second derivative of the virtual internal work with respect to $\underset{\sim}{c}, d\underset{\sim}{c} = \left\{\Delta\alpha_0^{i}, \Delta\alpha_n^{i}, \Delta\beta_n^{i}, \Delta\gamma_0^{i}, \Delta\gamma_n^{i}, \Delta\delta_n^{i}, \Delta\lambda_j\right\}, F_{\underset{\sim}{\text{Ext}}}(= \partial W_{\text{Ext}}/\partial\underset{\sim}{c})$, is the

derivative of the virtual external work with respect to $\underset{\sim}{c}$, and $\underset{\sim}{F}_{\text{Int}}(=\partial W_{\text{Int}}/\partial \underset{\sim}{c})$ is the derivative of the virtual internal work with respect to $\underset{\sim}{c}$. The nodal force $\underset{\sim}{F}(=\underset{\sim}{F}_{\text{Int}}(\partial \underset{\sim}{c}/\partial \underset{\sim}{u}))$ can be calculated from $\underset{\sim}{F}_{\text{Int}}$ and $\partial \underset{\sim}{u}/\partial \underset{\sim}{c}$. It should be noted that the derivatives with respect to $\underset{\sim}{c}$ and $\mathrm{d}\underset{\sim}{c}$ yield the same result.

Pressure loading is modeled as an external force to expand the tube. The external work done by a pressure p applied to the inside of the tube is equal to:

$$\delta W^{P}_{\text{Ext}} = \sum_{i=1}^{I} \int_{L^i_p} p\hat{n}^i \delta(\Delta \underset{\sim}{u}^i) r^i \mathrm{d}L^i_p = \sum_{i=1}^{I} \int_{L^i_p} p\hat{n}^i \frac{\partial(\Delta u^i)}{\partial \underset{\sim}{c}} \delta \underset{\sim}{c} r^i \mathrm{d}L^i_p \tag{35}$$

where $\delta(\Delta \underset{\sim}{u}^i)$ is the incremental virtual displacement vector having two components $\delta(\Delta w^i)$ and $\delta(\Delta u^i)$, $\hat{n}^i$ is the unit outward normal to the segment L^i_p.

The variation of the virtual external work, equation (35), with respect to $\underset{\sim}{c}$ is:

$$\underset{\sim}{F}^{P}_{\text{Ext}} = p\sum_{i=1}^{I} \int_{L^i} \hat{n}^i \frac{\partial(\Delta \underset{\sim}{u}^i)}{\partial \underset{\sim}{c}} r^i \mathrm{d}L^i_p \tag{36}$$

Owing to the follower forces effect (Hibbitt, 1979), the load stiffness matrix is:

$$\underset{\approx}{K}^{P}_{\text{Ext}} = p\sum_{i=1}^{I} \int_{L^i_p} \left(\frac{\partial(\hat{n}^i)}{\partial \underset{\sim}{c}} \frac{\partial(\Delta \underset{\sim}{u}^i)}{\partial \underset{\sim}{c}} + \hat{n}^i \frac{\partial^2(\Delta \underset{\sim}{u}^i)}{\partial^2 \underset{\sim}{c}} \right) r^i \mathrm{d}L^i_p \tag{37}$$

equations (36) and (37) will appear on the right-hand and left-hand side of the Newton-Raphson expression, equation (34), respectively, namely:

$$\left[\underset{\approx}{K} + \underset{\approx}{K}^{p}_{\text{Ext}} \right] [\mathrm{d}\underset{\sim}{c}] = \underset{\sim}{F}_{\text{Ext}} + \underset{\sim}{F}^{p}_{\text{Ext}} - \underset{\sim}{F}_{\text{Int}} \tag{38}$$

.

6.2 Axial loading model

Simultaneous application of axial force with internal pressure is critical to improving material shaping abilities for deeper draw configurations and higher expansion in localized regions. Axial compressive feed F is modeled as an external force applied to both ends of the tube as follows:

$$\delta W^{A}_{\text{Ext}} = (-1)^k F \hat{t}^i \delta(\Delta \underset{\sim}{u}^i)\Big|_{i=1,k=0}^{i=\text{nseg},k=1} = (-1)^k F \hat{t}^i \frac{\partial(\Delta u^i)}{\partial \underset{\sim}{c}} \delta \underset{\sim}{c}\Big|_{i=1,k=0}^{i=\text{nseg},k=1} \tag{39}$$

where $\hat{t}^i$ is the unit tangent vector along the segment L^i_p and nseg is total number of segments. Since, the force is compressive at both ends, when $i = 1$ (i.e. first segment), $k = 0$, and when i = nseg (i.e. last segment), $k = 1$.

6.3 Displacement stroke model

The displacement stroke at both ends of the tube is included in the equilibrium equation using Lagrange Multiplier technique. The axial stroke is specified in the u direction, along the length of the tube.

For the left end of the tube ($i = 1$):

$$u|_{s=0,i=1} = u^* \quad \Rightarrow \left(\gamma_0^j + \sum_{n=1}^{N^i} \gamma_n^j \cos \frac{n\pi s_i}{l_i^0} + \sum_{n=1}^{N^i} \delta_n^j \sin \frac{n\pi s_i}{l_i^0} \right) \Bigg|_{s=0,i=1} = u^*$$

$$\Rightarrow \quad \gamma_0^1 + \sum_{n=1}^{N^1} \gamma_n^1 = u^* \Rightarrow \quad \gamma_0^1 + \sum_{n=1}^{N^1} \gamma_n^1 - u^* = 0 \tag{40}$$

For the right end of the tube (i = nseg):

$$u|_{s=l,i=\text{nseg}} = -u^*$$

$$\Rightarrow \left(\gamma_0^j + \sum_{n=1}^{N^i} \gamma_n^j \cos \frac{n\pi s_i}{l_i^0} + \sum_{n=1}^{N^i} \delta_n^j \sin \frac{n\pi s_i}{l_i^0} \right) \Bigg|_{s=l,i=\text{nseg}} = -u^*$$

$$\Rightarrow \gamma_0^{\text{nseg}} + \sum_{n=1}^{N^{\text{nseg}}} (-1)^n \gamma_n^{\text{nseg}} = -u^* \Rightarrow \quad \gamma_0^{\text{nseg}} + \sum_{n=1}^{N^{\text{nseg1}}} (-1)^n \gamma_n^{\text{nseg}} + u^* = 0 \tag{41}$$

Equations (40) and (41) are incorporated into the equilibrium equation using two Lagrange multipliers.

6.4 Frictional contact model

To model the tube-die frictional contact correctly, the following two conditions are checked during equilibrium iteration:

(1) penetration of the tube nodes into the die; and

(2) nodal contact forces becoming tensile at the contact boundary (separation).

Once the penetration of the contact nodes into the die has been detected, the penetrated nodes are returned to the die surface and constrained to stay on the die surface for the remainder of the equilibrium iterations. The nodes, which are returned to the die surface, are constrained to move only tangent to the die surface and only condition 2 stated above could cause the contacting node to be separated from the die surface. Figure 7 shows the schematic of a typical contact check during the Newton-Raphson equilibrium iteration.

The external work done by the frictional contact is added into the virtual work principle, equation (31), as following:

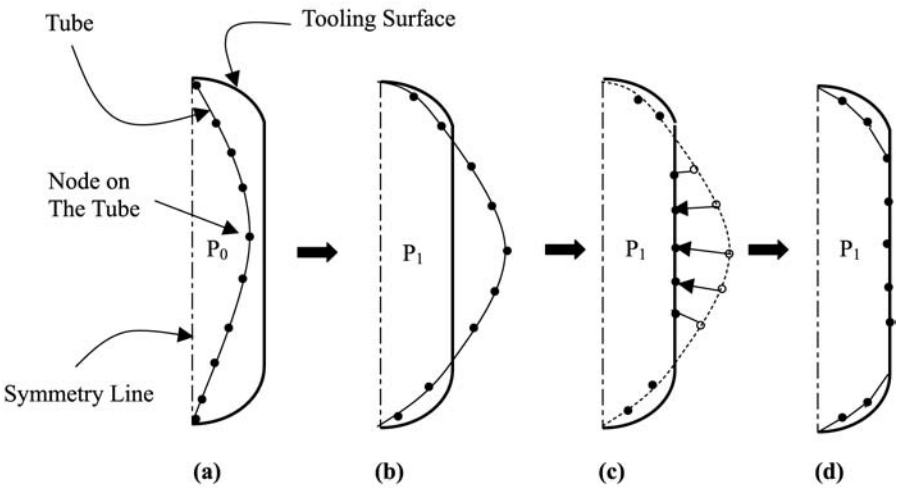

Figure 7.
A schematic of tube-die contact check

Note: (a) shows the tube and the die, (b) shows initial penetration of some of the contact nodes as internal pressure increases from P_0 to P_1, (c) shows how contact nodes are returned to the die surface, and finally (d) shows how the equilibrium shape is reached after several iterations

$$\sum_{i=1}^{I}\int_{L^i}\left(\sigma_s^j\delta\varepsilon_s^i+\sigma_{r_i}^j\delta\varepsilon_{r_i}^i\right)r^i dL^i+\sum_{j=1}^{J+2}\lambda_j\delta C_j=$$

$$\left(-1\right)^k F\hat{t}^i\delta(\Delta\underset{\sim}{u}^i)\Big|_{i=1,k=0}^{i=\mathrm{nseg},k=1}+p\sum_{i=1}^{I}\int_{L^i}\hat{n}^i\frac{\partial(\Delta\underset{\sim}{u}^i)}{\partial\underset{\sim}{c}}r^i\mathrm{d}L_p^i \tag{42}$$

$$+\sum_{i=1}^{I}\int_{L^i}\tau_i\delta(\Delta\underset{\sim}{u}^i)r^i\mathrm{d}L_p^i$$

where τ_i is the traction on the surface of the tube and $\delta(\Delta\underset{\sim}{u}^i)$ is the virtual incremental displacement of the contacting nodes. The two extra Lagrange multipliers λ_j account for the displacement strokes at the two ends of the tube.

7. Numerical algorithm

In order to improve convergence, a special algorithm is introduced (Figure 8). For every load increment, the non-penetration contact condition is checked initially. If contact is detected, contact nodes on the tube meridian are projected onto the die surface along the normal vector. The trial displacements are next updated based on Newton-Raphson procedure. For each trial set of contacting and non-contacting nodes, equilibrium iteration is performed. Within this force equilibrium iteration, the internal force is calculated. The signs of the sheet normal force at contact points are checked so that the nodes having non-compressive force are released. After equilibrium is satisfied, the

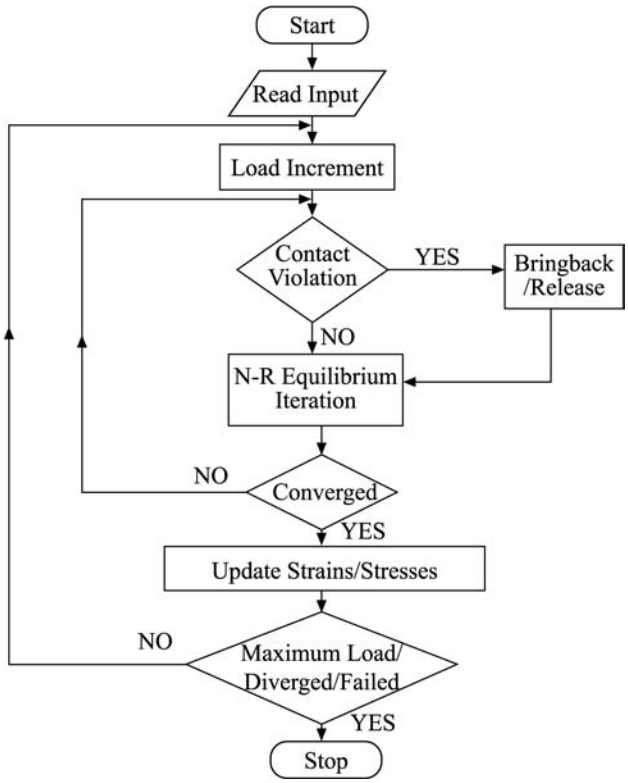

Figure 8.
Flow chart for AXHD program

strains and stresses are updated and failure based on FLC fracture criteria is checked. The program stops when maximum load step is reached or failure is detected.

8. Fracture criteria

FLC equations based on the onset of shear instability and experimental measurements are incorporated into the program as fracture criteria to detect the onset of failure. The FLC based on the onset of local shear instability, using Hosford yield criterion and critical shear stress under plane strain (Lee and Kim, 1989), is given by:

$$\varepsilon_1^* = 2^{-(1/n)}\left[1+\left(\frac{1}{|\beta|}\right)^a + R\left|1-\frac{1}{\beta}\right|^a\right]^{(na-n-1)/na}\left[1+R\left(1-\frac{1}{\beta}\right)^{-1}\left|1-\frac{1}{\beta}\right|^a\right]^{-1}$$
$$(1+|\alpha|^a+R|1-\alpha|^a)^{(1-na+n)/na}[1+R(1-\alpha)^{-1}|1-\alpha|^a](2+\rho)^{1/n} \quad (43)$$
$$(1+\rho)^{-1/2n}\left(\varepsilon_{1p}^*\right)$$

where parameters α, ρ, β, a, n, R, ε_1^* and ε_{1p}^* are defined in the Nomenclature.

The effects of thickness, surface roughness and strain gradient through the thickness are not accounted for in the above equation.

9. Numerical results

The AXHD (Axisymmetric Hydroforming) program has been written and validated with experimental data and ABAQUS finite element model using the following two examples. In each example, due to the lack of experimental data, a friction coefficient of 0.1 was used to account for the frictional contact between the tube and the die corner. Also, in these examples the sensitivity of the result to the value of the friction coefficient was not studied.

9.1 Bulging of an anisotropic aluminum tube

This example concerns the bulging of a straight aluminum tube using an Interlaken tube hydroforming press at Michigan State University. The aluminum tube used in the bulging experiment was 8.0 in. (203 mm) long, and had an outside diameter of 2.0 in. (50.8 mm), and a wall thickness of 0.049 in. (1.24 mm). The measured mechanical properties for the aluminum 6061-T4 tube are given in Table I. In the bulging test, the straight tube was first placed horizontally into the bottom die cavity and then steel plungers were inserted from each side to seal the two ends of the tube. Upon closing the top die, the tube was clamped and then filled with water. The goal of the experiment was to linearly increase the fluid pressure inside the aluminum tube to a maximum value of 2,030 psi, while axially compressing the two ends of the tube. This pressure-axial stroke loading condition was by no means an optimized one, but was rather found to work well for this geometry by running several bulging tests. While it was possible with good control to linearly increase the fluid pressure to its maximum value of 2,030 psi, it was not possible to apply equal amount of axial stroke to the ends of the tube during the bulging experiment. At the end of the bulging process, the length of the deformed tube was measured again and it was found to be 0.236 in. (6.0 mm) shorter than its original length of 8.0 in.. It is believed that this shortening in the length of the tube was caused by a combination of the axial feed action (to stop fluid leaking from the ends of the tube), and the natural draw-in of the tube as it expanded inside the die cavity. For simplicity, however, in the numerical simulations with AXHD and ABAQUS codes it was decided to apply an equal amount of 0.118 in. (3.0 mm) axial stroke to each end of the tube.

The deformed shape and strain results obtained from the AXHD code (written based on current formulation) were compared with the results of the commercial FEM code ABAQUS and experimental measurements. To assess the effect of the anisotropy of the aluminum tube on strain distribution along the length of the tube, the ABAQUS FEM code was run with the following yield functions:

- von Mises (isotropic); and
- Hill (1948) (transverse anisotropy)

Table I.
Material properties of the aluminum and steel tubes used in the simulations

Material type	Young's modulus (psi)	Poisson ratio	Yield stress (psi)	*R*-value	*K*-value (psi)	*N*-value	ε_0
Aluminum 6061-T4	1.03×10^7	0.33	18,730	0.82	69,183	0.2646	0.0
Steel DP600	3.15×10^7	0.3	51,040	1.0	143,260	0.182	0.0

All finite element simulations were performed with ABAQUS/Explicit code, using plane stress axisymmetric (SAX1) and four-node shell elements with reduced integration (S4R). Figure 9 shows the intermediate shapes of the deformed tube predicted by the AXHD code at various internal pressure levels. Table II shows the information about the number of Fourier series terms, Gauss integration points, and contact points used in these simulations. Similar to the experiment, the tube was pressurized to the maximum pressure level of 2,030 psi while being axially compressed by a maximum stroke of 0.118 in. (3.0 mm) at each end. The predicted deformed shape of the tube at the maximum pressure of 2,030 psi was compared against the actual deformed shape of the tube. The maximum radius of the deformed tube was predicted to be 1.17 in. (29.72 mm), while that of the actual tube was measured to be 1.22 in. (31.0 mm). This corresponds to an underestimation of 4.1 percent for the maximum deformed tube radius.

Corresponding distribution of hoop and axial strains along the length of the tube are shown in Figures 10 and 11. As expected, the maximum hoop and axial strains occur in the middle of the bulged tube and they are 17.54 and −7.4 percent, respectively.

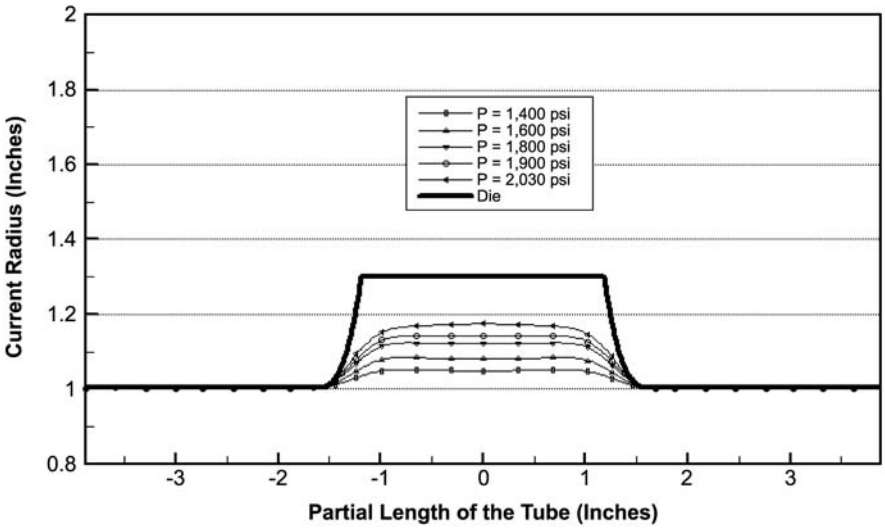

Note: The aluminum 6061-T4 tube had the following dimensions: $t_o = 0.049"(1.24\,mm)$, $d_o = 2.0"(50.8\,mm)$, $L_o = 8.0"(203\,mm)$

Figure 9.
Tube radius vs length at different bulging pressure. The aluminum 6061-T4 tube had the following dimensions: $t_o = 0.049$ in. (1.24 mm), $d_o = 2.0$ in. (50.8 mm), $L_o = 8.0$ in. (203 mm)

Material type	Nos. straight elements	Nos. terms in displacement series	Nos. gauss points along the segment	Nos. gauss points through the thickness	Nos. contact points per segment
Aluminum 6061-T4	8 and 12	5	10	5	41
Steel DP600	8	6	12	7	41

Table II.
Fourier series terms, gauss integration points and contact points used in AXHD

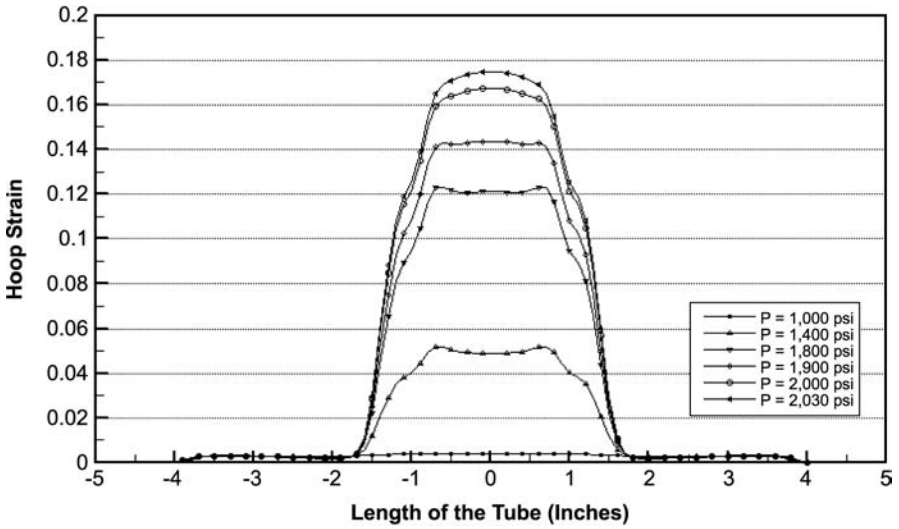

Figure 10.
Hoop strain along the tube length at different bulging pressures (aluminum)

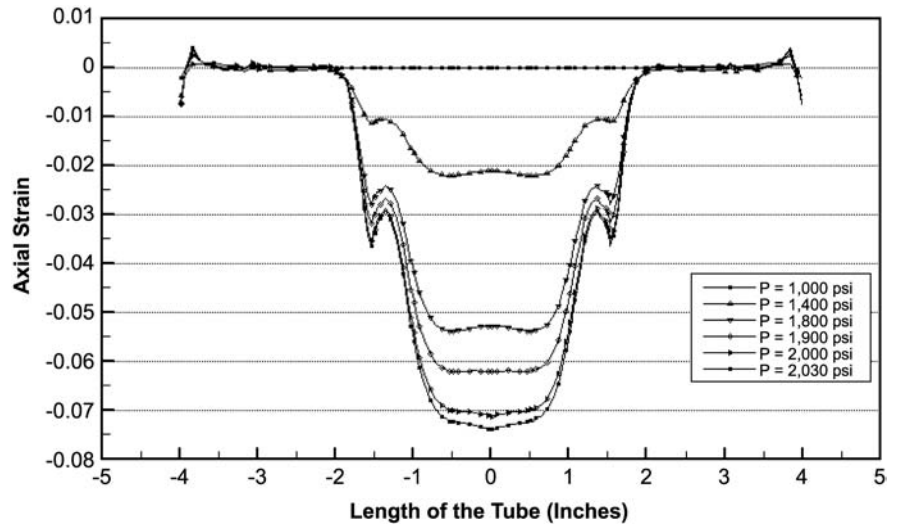

Figure 11.
Axial strain along the tube length at different bulging pressures (aluminum)

Figure 12 shows the history of the thinning of the tube at the maximum bulge point (middle of the tube) as a function of the applied pressure. Thinning of the tube accelerates exponentially beyond the pressure level of 1,000 psi. The thinning strain at the pressure level of 2,030 psi is around 10 percent.

Figures 13 and 14 show a comparison of hoop and axial strain distributions predicted with AXHD and ABAQUS/Explicit code using the nonlinear axisymmetric element (SAX1) and four-node shell element with reduced integration (S4R). The number of SAX1 elements used for the axisymmetric analysis was 80 while that for S4R elements was 1,176. The hoop strain distribution predicted by the AXHD code,

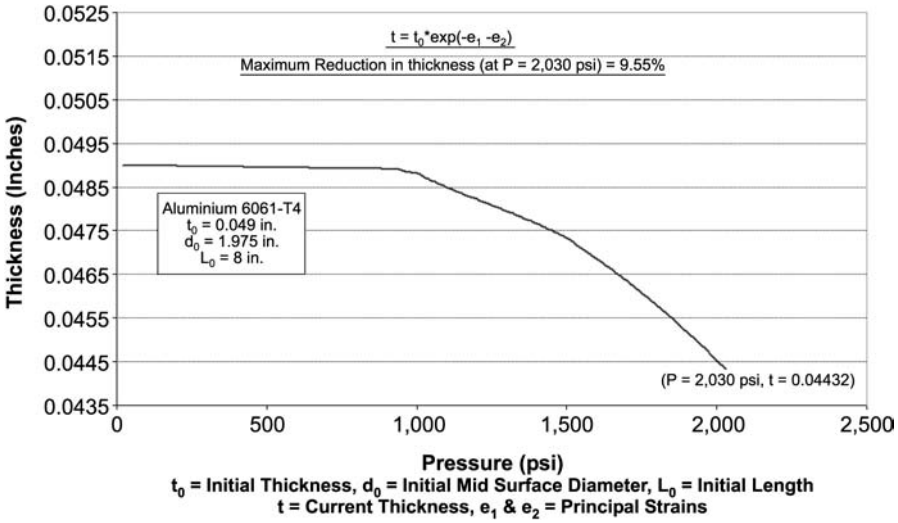

Figure 12.
Thickness vs pressure (at maximum bulge point)

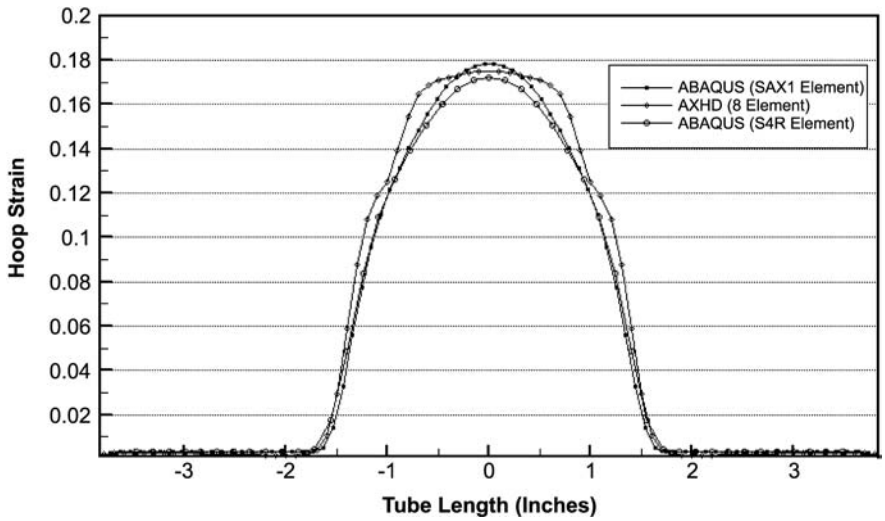

Figure 13.
Hoop strain (AXHD vs ABAQUS/Explicit)

using eight straight segments, matches those of ABAQUS very well, despite the fact that a S4R shell element takes into account shear deformation. The axial strain distribution predicted by the AXHD code matches those of ABAQUS very well too. The two spikes (at ± 1.65 in.) shown in Figure 14 for the ABAQUS code are attributed to the tube-die contact in the region where the die cavity starts (Figure 9). In this region the tube bends over the die radius and develops a large axial strain. There is a slight discrepancy between ABAQUS and AXHD code predictions in this region. This could partly be attributed to neglecting $u_{,S}$ and $u_{,SS}$ terms in the axial curvature equation (equation (A10) in Appendix), which lead to the more simplified expression for the

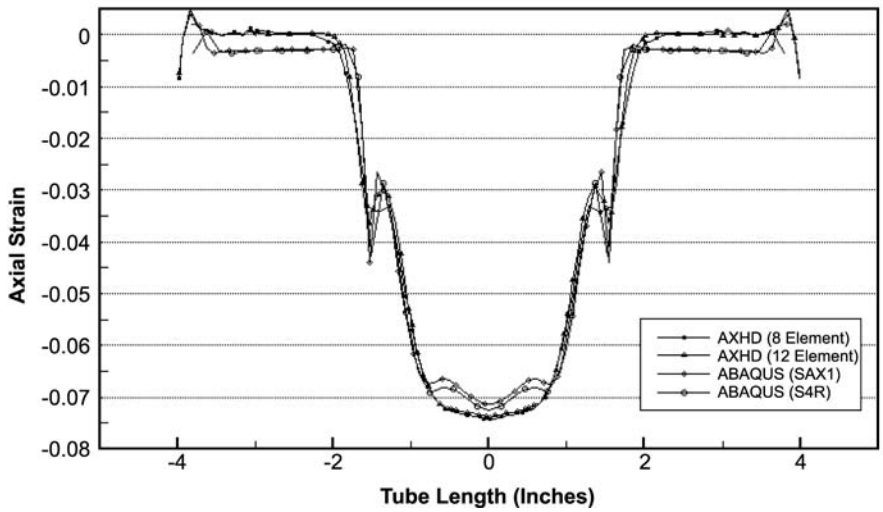

Figure 14.
Axial strain (AXHD vs ABAQUS/Explicit)

axial curvature in equation (16). However, by increasing the number of straight segments used in the AXHD code from 8 to 12, this spike in the axial strain was better captured. This implies that due to the small radius of the die corner more straight segments were needed in order to accurately capture the strain gradient in the curved region of the tube.

Figure 15 shows a comparison of the measured and predicted hoop strain distributions. In the numerical simulations isotropic and transversely anisotropic material models were assumed. Hill's yield criterion accounting for the transverse anisotropy, equation (25), was used with ABAQUS' SAX1 and S4R shell elements and

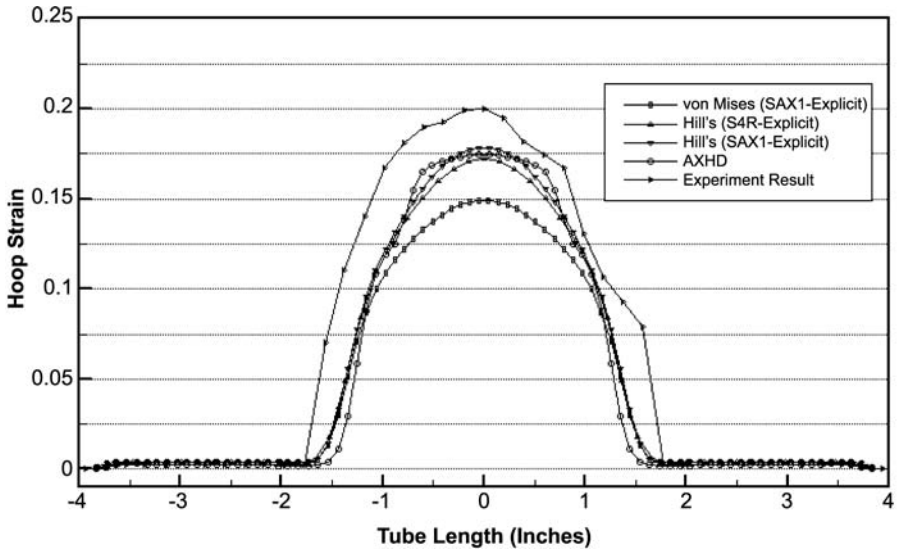

Figure 15.
Hoop strain predictions with ABAQUS using different yield functions and elements and comparison with experimental strains

compared with AXHD results. As expected, the isotropic material model (von Mises) significantly underestimated the magnitude of the maximum hoop strain (14.9 percent). Those models (Hill's SAX1, S4R and AXHD) accounting for the transverse anisotropy of the tube predicted a maximum strain of 17.4 percent, which was a drastic improvement over the von Mises' prediction. Despite the improvement, all three models underestimated the measured maximum hoop strain of 20 percent. Plate 1 shows the deformed aluminum tube after the bulging experiment.

The large difference observed between the experimental and FEA results in Figure 15 could be attributed to several factors, of which the most significant is the planar anisotropy of the extruded aluminum tube. This will be verified in the future by using Barlat Yld96 yield function (Barlat *et al.*, 1997) to model tube bulging. A second explanation would be that the maximum attainable pressure in the tube hydroforming equipment was 30,000 psi, while the bulging pressure for the aluminum tube was only 2,030 psi. Therefore, a small error of only 0.5 percent (150 psi) in the pressure reading from the equipment could have caused a significant change in strain and deformation results. That is, the actual pressure being somewhat larger than 2,030 psi could have caused a large discrepancy in the experimentally measured strain results. A third explanation would be that the 3 mm axial feed per side boundary condition used in the simulations may have been larger than the actual axial feed in the bulged tube. If true, this would certainly cause an underestimation in the predicted maximum hoop strain. Finally, the slight shift to the left in the experimental curve, in Figure 15, could have been caused by an uneven application of the axial feed to the two ends of the bulged tube during the experiment. Next, the bulging of an isotropic steel tube will be discussed to better assess the accuracy of the formulation.

Plate 1.
Axisymmetrically bulged aluminum tube using 2,030 psi internal pressure

9.2 Bulging of an isotropic steel tube

This example is concerned with the optimized bulging of an isotropic straight steel tube under controlled pressure and displacement stroke. The steel tube is 8.66 in. (220 mm) long with an outside diameter of 2.36 in. (60 mm) and with a wall thickness of 0.05787 in. (1.47 mm). The material properties for the hot-dip galvanized DP600 (HG/Z140) steel tube are given in Table I.

The axial stroke vs pressure loading history and experimental results for this simulation are obtained from Asnafi (1999). The FLC, based on the onset of shear instability (Lee and Kim, 1989) and experimental measurements (Asnafi, 1999; Asnafi and Skogsgardh, 2000) are also used as fracture criteria. As shown in the figures described below, the simulation results from the AXHD code are in close agreement with the experimental results reported by Asnafi (1999) and Asnafi and Skogsgardh (2000) for this isotropic material.

Figure 16 shows the intermediate shapes of the bulged steel tube at various internal pressure levels. Those deformed shapes were predicted by the AXHD code using 12 straight elements and the displacement stroke-internal pressure history shown in Figure 17, obtained from the analytical equations given by Asnafi (1999) in order to maintain a proportional axial to hoop strain ratio of -0.5. The final displacement stroke was 0.24 in. (6.1 mm) at the maximum pressure level of 5,220 psi in the tube bulging process.

Figures 18 through 20 show the predictions of the evolution of hoop strain, axial strain and the maximum thickness reduction as a function of the internal pressure by the AXHD code. The maximum thickness strain at the maximum pressure level of 5,220 psi is 15.57 percent. The maximum hoop and axial strains predicted by the AXHD code were 28 and -10.9 percent, respectively. These predicted values

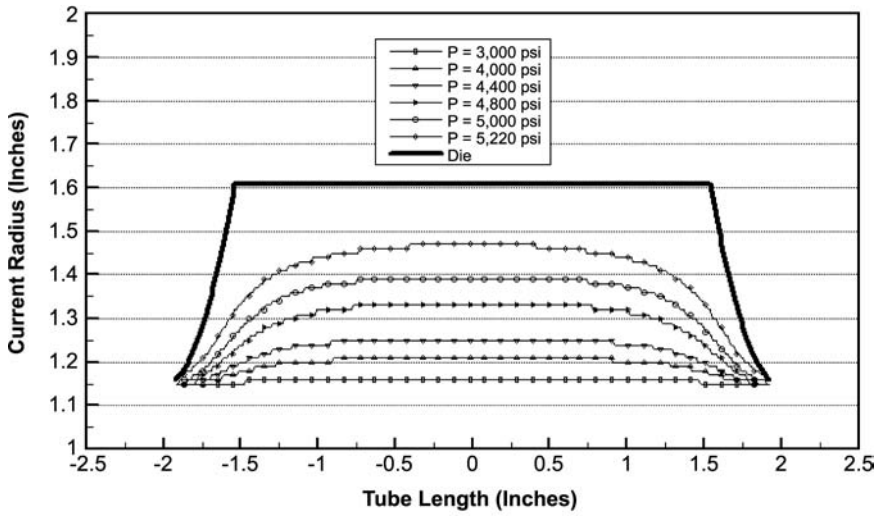

Figure 16.
Intermediate shapes of the bulged steel tube.

Note: The hot-dip galvanized DP600 (HG/Z140) steel tube had the following dimensions: $t_o = 0.05787"(1.47\,mm)$, $d_o = 2.36"(60\,mm)$, $L_o = 8.66"(220\,mm)$

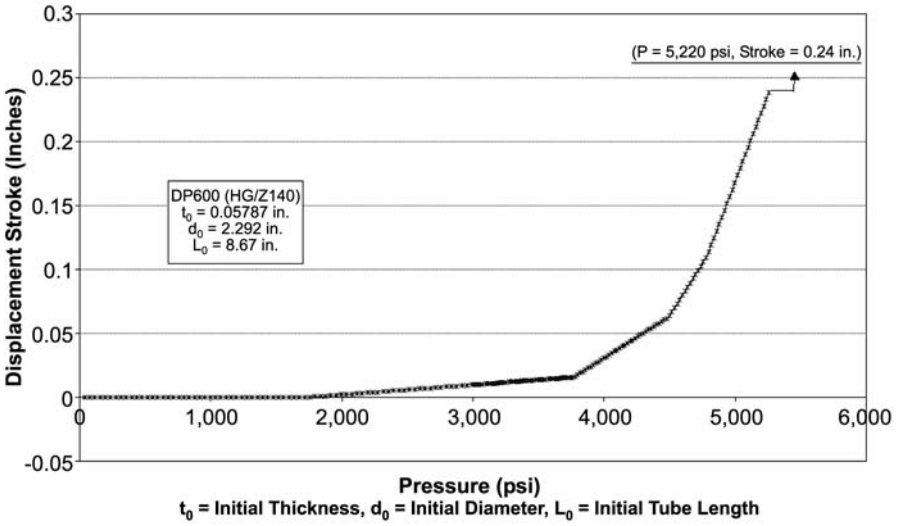

Source: Asnafi (1999)

Figure 17.
Pressure vs axial feed (stroke) curve used for bulging the steel tube

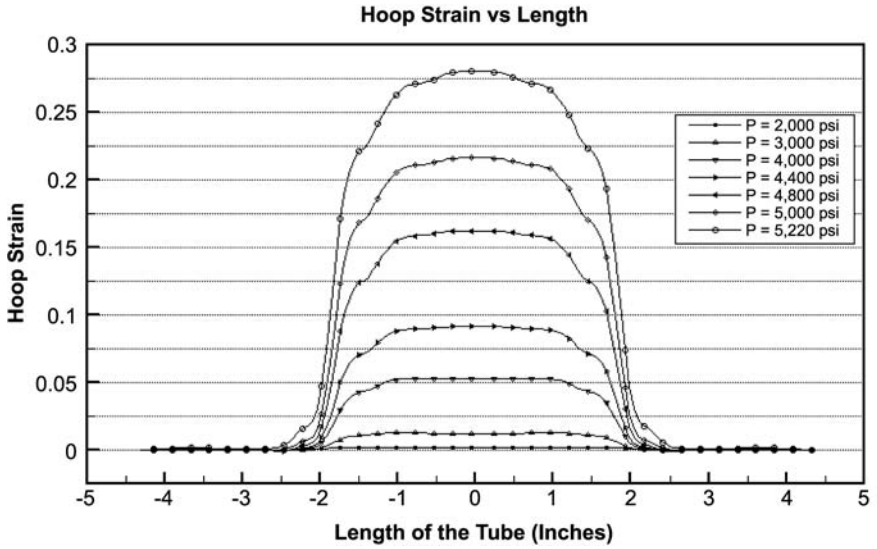

Figure 18.
Hoop strain along the tube length at different bulging pressures (steel)

compared very well with the measured hoop and axial strains of 29 and −10 percent reported by Asnafi (1999) and Asnafi and Skogsgardh (2000).

Finally, Figure 21 shows the major and minor strains predicted by the AXHD code along the length of the hydroformed steel tube at the maximum pressure of 5,220 psi. These predicted strains are compared with the experimentally measured forming limit strains reported by Asnafi (1999) and the FLC calculated based on the shear instability

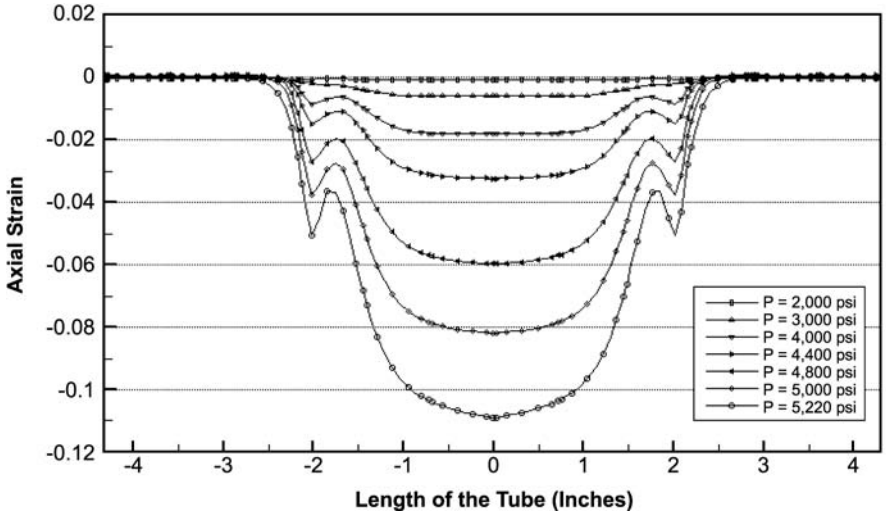

Figure 19.
Axial strain along the tube length at different bulging pressures (steel)

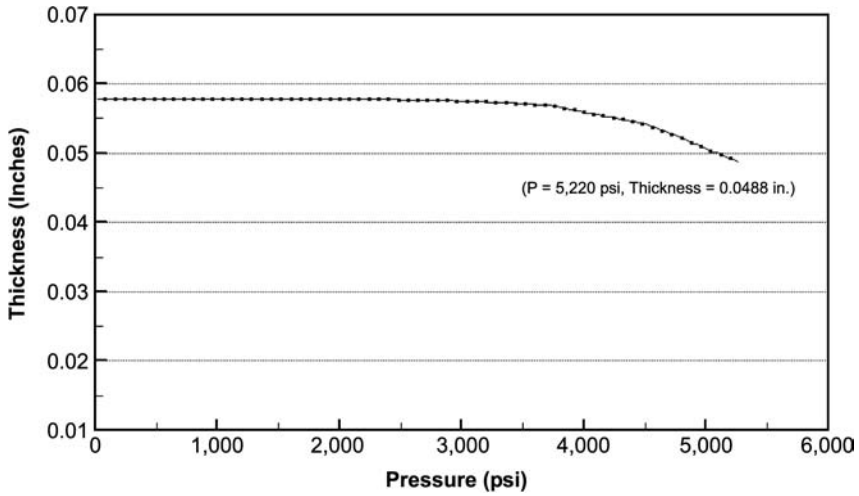

Figure 20.
Thickness vs pressure (at maximum bulge point)

criterion (Lee and Kim, 1989). FLCs correspond to the maximum strains that a material can safely undergo prior to failure (e.g. tearing) under various deformation conditions. Referring to Asnafi's FLC in Figure 21, it is clear that the steel tube will cross the FLC and fail by tearing once major and minor strains reach about 0.30 and -0.11, respectively. The FLC curve based on the shear instability however predicts major and minor strains of about 0.325 and -0.11 prior to tearing. For engineering design it is better to use the more conservative curve. Overall, it seems that the FLC is a useful tool for estimating the critical strains at the onset of fracture for isotropic steel tubes.

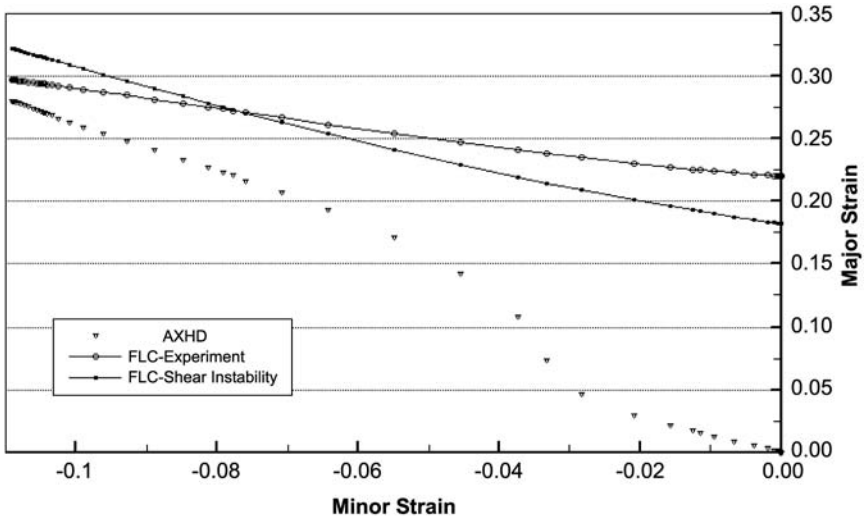

Note: These strains are compared with the experimentally measured and theoretically (shear instability) calculated forming limit curves (FLC)

Figure 21.
The major and minor strains predicted by the AXHD code along the length of the hydroformed steel tube at the maximum pressure of 5,220 psi

10. Conclusions

In the present study, an axisymmetric tube hydroforming finite element analysis program was developed. Fourier series interpolation functions, which reduce the size of the global stiffness matrix and the number of variables considerably, were employed for approximating the displacements. The computer program (AXHD) written based on this formulation is very efficient in predicting the deformations for the free-forming stage of tube hydroforming under simultaneous action of internal pressure and displacement stroke. Failure model (FLC) based on shear instability was incorporated into the code to predict the onset of fracture for the steel tube. The hoop and axial strains predicted with AXHD code compared excellently with those from ABAQUS FEM code using plane stress axisymmetric (SAX1) and four-node shell (S4R) elements. However, in the case of aluminum, the numerically predicted maximum hoop strain underestimated the actual hoop strain measured from the tube bulging experiment. This was attributed to several factors of which the planar anisotropy of the aluminum tube was deemed to be the most important. To verify this, simulations with planar anisotropic yield functions are planned for the future. It is also planned to extend this axisymmetric code to a general three-dimensional (3D) code in order to perform post-bifurcation analysis of tube hydroforming process.

References

Anon (1997), "Hydroforming technology", *Advanced Material Process*, Vol. 151 No. 5, pp. 50-3.

Asnafi, N. (1999), "Analytical modelling of tube hydroforming", *Thin-Walled Structures*, Vol. 34, pp. 295-330.

Asnafi, N. and Skogsgardh, A. (2000), "Theoretical and experimental analysis of stroke-controlled tube hydroforming", *Materials Science and Engineering*, Vol. A279, pp. 95-110.

Aue-U-Lan, Y., Ngaile, G. and Altan, T. (2004), "Optimizing tube hydroforming using process simulation and experimental verification", *J. Mater. Process. Tech.*, Vol. 146 No. 1, pp. 137-43.

Aydemir, A., de Vree, J.H.P., Brekelmans, W.A.M., Geers, M.G.D., Sillekens, W.H. and Werkhoven, R. (2005), "An adaptive simulation approach designed for tube hydroforming processes", *J. Mater. Process. Tech.*, Vol. 159 No. 3, pp. 303-10.

Barlat, F., Maeda, Y., Chung, K., Yanagawa, M., Brem, J.C., Hayashida, Y., Lege, D.J., Matsui, K., Murtha, S.J., Hattori, S., Becker, R.C. and Makosey, S. (1997), "Yield function development for aluminum alloy sheets", *J. Mech. Phys. Solids*, Vol. 45, pp. 1727-63.

Berg, J.H. and Hora, P. (1996), "Simulation of complex hydroforming processes using an explicit code with a new shell formulation", paper presented at the 3rd International Conference: Numerical Simulation of 3D Sheet Metal Forming Processes - Verification of Simulations with Experiments, Dearborn, Michigan, September 29-October 3, pp. 330-5.

Corona, E. (2004), "A simple analysis for bend-stretch forming of aluminum extrusions", *Int. J. Mech. Sci.*, Vol. 46, pp. 433-48.

Dohmann, F. and Hartl, Ch. (1996), "Hydroforming: a method to manufacture light-weight parts", *J. Mater. Process. Tech.*, Vol. 60, pp. 669-76.

Fann, K.J. and Hsiao, P.Y. (2003), "Optimization of loading conditions for tube hydroforming", *J. Mater. Process. Tech.*, Vol. 140, pp. 520-4.

Hama, T., Asakawa, M. and Makinouchi, A. (2004a), "Investigation of factors which cause breakage during the hydroforming of an automotive part", *J. Mater. Process. Tech.*, Vol. 150 Nos 1/2, pp. 10-7.

Hama, T., Asakawa, M., Fukiharu, H. and Makinouchi, A. (2004b), "Simulation of hammering hydroforming by static explicit FEM", *Iron and Steel Institute of Japan*, Vol. 44 No. 1, pp. 123-8.

Hama, T., Asakawa, M., Fuchizawa, S. and Makinouchi, A. (2003), "Analysis of hydrostatic tube bulging with cylindrical die using static explicit FEM", *Materials Transactions*, Vol. 44 No. 5, pp. 940-5.

Hibbitt, H.D. (1979), "Some follower forces and load stiffness", *Int. J. Num. Mech. Engng*, Vol. 14, pp. 937-41.

Hill, R. (1948), "Theory of the yielding and plastic flow of anisotropic metals", *Royal Soc. London Proc.*, Vol. 193A, p. 281.

Hsu, T.C. and Chu, C.H. (1995), "A finite element analysis of sheet metal forming process", *J. Mater. Process. Tech.*, Vol. 54, pp. 70-5.

Hsu, Q.C. (2003), "Theoretical and experimental study on the hydroforming of bifurcation tube", *J. Mater. Process. Tech.*, Vol. 142 No. 2, pp. 367-73.

Hu, P., Liu, Y.Q., Li, Y.X. and Lian, J. (1997), "Rigid viscoplastic finite element of the gas-pressure constrained bulging of superlastic circular sheets into cone disk shape dies", *Int. J. Mech. Sci.*, Vol. 39 No. 4, pp. 487-96.

Hwang, Y.M. and Altan, T. (2003), "Finite element analysis of tube hydroforming processes in a rectangular die", *Finite Element in Analysis and Design*, Vol. 39 No. 11, pp. 1071-82.

Hwang, Y.M. and Altan, T. (2004), "Process fusion: tube hydroforming and crushing in a square die", *Proceedings of the Institution of Mechanical Engineers – Part B – Journal of Engineering Manufacture*, Vol. 218 No. 2, pp. 169-74.

Imaninejad, M., Subhash, G. and Loukus, A. (2004), "Influence of end-conditions during tube hydroforming of aluminum extrusions", *Int. J. Mech. Sci.*, Vol. 46 No. 8, pp. 1195-212.

Johnson, K.I., Nguyen, B.N., Davies, R.W., Grant, G.J. and Khaleel, M.A. (2004), "Numerical process control method for circular-tube hydroforming prediction", *Int. J. Plasticity*, Vol. 20 No. 6, pp. 1111-37.

Kaya, S., Gorospe, I. and Altan, T. (2002), "Preforming and expansion of an aluminum alloy in tube hydroforming – comparison of FEA predictions with existing experimental data", paper presented at NAMRC XXX, Purdue University, West Lafayette, IN, pp. 21-4.

Kim, J. and Kang, B.S. (2004), "Analytical approach to bursting failure prediction in tube hydroforming based on plastic instability", *Advances in Engineering Plasticity and its Applications, Parts 1 and 2 – Key Engineering Materials*, Vol. 274/276, pp. 601-6.

Kim, J., Kang, B.S. and Choi, H.H. (2002), "Numerical analysis and design for tube hydroforming process by rigid-plastic finite element method", *Transactions of NAMRI/SME*, Vol. XXX, pp. 127-34.

Kim, J., Kang, S.J. and Kang, B.S. (2003), "A prediction of bursting failure in tube hydroforming processes based on ductile fracture criterion", *International Journal of Advanced Manufacturing Technology*, Vol. 22 Nos 5/6, pp. 357-62.

Kim, J., Kang, B.S., Hwang, S.M. and Park, H.J. (2004), "Numerical prediction of bursting failure in tube hydroforming by the FEM considering plastic anisotropy", *J. Mater. Process. Tech.*, Vol. 153/54, pp. 544-9.

Kobayashi, S., Oh, S.I. and Altan, T. (1989), *Metal Forming and the Finite Element Method*, Oxford University Press, New York, NY.

Kulkarni, A., Biswas, P., Narasimhan, R., Luo, A.A., Mishra, R.K., Stoughton, T.B. and Sachdev, A.K. (2004), "An experimental and numerical study of necking initiation in aluminium alloy tubes during hydroforming", *International Journal of Mechanical Sciences*, Vol. 46 No. 12, pp. 1727-46.

Lang, L.H., Yuan, S.J., Wang, X.S., Wang, Z.R., Fu, Z., Danckert, J. and Nielsen, K.B. (2004), "A study on numerical simulation of hydroforming of aluminum alloy tube", *J. Mater. Process. Tech.*, Vol. 146 No. 3, pp. 377-88.

Lee, D.N. and Kim, Y.K. (1989), "Forming limit diagrams for stainless steel clad aluminium sandwich sheets", internal report, Seoul National University.

Lin, F.C. and Kwan, C.T. (2004), "Application of abductive network and FEM to predict an acceptable product on T-shape tube hydroforming process", *Computers & Structures*, Vol. 82 Nos 15/16, pp. 1189-200.

Liu, S.D., Mueleman, D. and Thompson, K. (1998), "Analytical and experimental examination of tubular hydroforming limits", SAE Technical Paper No. 980449, February 23-26, pp. 139-50.

Longhouse, B. (1998), "Applied pressure sequence hydroforming", paper presented at the 3rd Annual Automotive Tube Fabricating.

Miller, J.E., Kyriakides, S. and Bastard, A.H. (2001a), "On bend-stretch forming of aluminum extruded tubes – I: experiments", *Int. J. Mech. Sci.*, Vol. 43, pp. 1283-317.

Miller, J.E., Kyriakides, S. and Corona, E. (2001b), "On bend-stretch forming of aluminum extruded tubes – II: analysis", *Int. J. Mech. Sci.*, Vol. 43, pp. 1319-38.

Morphy, G. (1997), "Hydroforming high strength steel tube for automotive structural applications using expansion", paper presented at SAE International Congress & Exposition.

Nagteggal, J.C. and Rebelo, N. (1988), "On the development of a general purpose finite element program for analysis of forming processes", *Int. J. Num. Methods Eng.*, Vol. 25, pp. 113-31.

Ni, C.M. (1994), "Stamping and hydroforming process simulation with a 3D finite element code", SAE Paper No. 940753, SAE SP-1021.

Noh, T.S. and Yang, D.Y. (1998), "A general formulation for hydroforming of arbitrarily shaped boxes and its application to hydroforming of an elliptic-circular box", *J. Manufacturing Science and Engineering*, Vol. 120, pp. 481-8.

Oh, S.I. (1982), "Finite element analysis of metal forming processes with arbitrarily shaped dies", *Int. J. Mech. Sci.*, Vol. 24 No. 8, pp. 479-93.

Papelnjak, T. (2004), "Numerical analyses of tube hydroforming by high internal pressure", *Strojniski Vestnik-Journal of Mechanical Engineering*, Vol. 50 No. 1, pp. 31-43.

Pourboghrat, F., Karabin, M.E., Becker, R.C. and Chung, K. (2000), "A hybrid membrane/shell method for calculating springback of anisotropic sheet metals undergoing axisymmetric loading", *Int. J. Plasticity*, Vol. 16, pp. 677-700.

Ray, P. and MacDonald, B.J. (2004), "Determination of the optimal load path for tube hydroforming processes using a fuzzy load control algorithm and finite element analysis", *Finite Elements in Analysis and Design*, Vol. 41 No. 2, pp. 173-92.

Srinivasan, T.M., Shaw, J.R. and Thompson, K. (1998), "Tubular hydroforming: correlation of experimental and simulation results", SAE Technical Paper No. 980448, Februrary 23-26, pp. 131-7.

Wang, N.M. and Budiansky, B. (1978), "Analysis of sheet metal stamping by a finite element method", *ASME J. Appl. Mechs.*, Vol. 45, pp. 73-82.

Wang, N.M. and Tang, S.C. (1988), "Analysis of bending effects in sheet forming operations", *Int. J. Num. Methods Eng.*, Vol. 25, pp. 253-67.

Appendix

Using the updated Lagrangian formulation discussed in Section 2 (Shell element model), a set of expressions were derived for the membrane strains, rotation of the normal vector, and the principal centerline curvatures of a shell element on the meridian of the tube. By using in these expressions the values of the displacements and curvatures of the shell at the previous time increment (i.e. $t = {}^{o}t$), one would recover incremental values of strains. And, by using in these expressions the values of displacements and curvatures of the shell at the initial state (i.e. $t = 0$) one would recover the total values of strains.

In this paper, the incremental strain is calculated by taking the difference between the total strain at the current (t) and the previous time increment (${}^{o}t$) as: $\Delta\varepsilon = \varepsilon(Y, t) - \varepsilon(Y, {}^{o}t)$. To calculate the total strain from the expressions shown in Section 2, one would need to set the original curvature of the straight segment equal to zero, i.e. $K_1 = 0$, and use for all kinematics parameters (i.e. displacements, and their derivatives) their total values (i.e. calculated based on their values at the current time t and $t = 0$).

Membrane strain

For a straight segment, by setting the curvature equal to zero, $K_1 = 0$, from equation (6) the total mid-surface stretch as a function of total displacements of the mid-surface of the shell and their derivative with respect to s becomes:

$$\lambda_1 = \left[(1 + u_{,S})^2 + w_{,S}^2\right]^{1/2} = \left[1 + u_{,S}^2 + 2u_{,S} + w_{,S}^2\right]^{1/2} \tag{A1}$$

or,

$$\lambda_1^2 = 1 + u_{,S}^2 + 2u_{,S} + w_{,S}^2 \tag{A2}$$

By substituting $\lambda_1 = 1 + \varepsilon_s^o$ into equation (A2), the following expression will result:

$$\varepsilon_s^o + \frac{1}{2}\left(\varepsilon_s^o\right)^2 = u_{,S} + \frac{1}{2}\left(u_{,S}^2 + w_{,S}^2\right) \tag{A3}$$

The above quadratic expression should be solved in order to obtain the mid-surface total strain, ε_s^o, as a function of the derivative of the mid-surface displacements. A simpler expression for ε_s^o was found by simply dropping the quadratic term $1/2(\varepsilon_s^o)^2$:

$$\varepsilon_s^o \approx u_{,S} + \frac{1}{2}\left(u_{,S}^2 + w_{,S}^2\right) \tag{A4}$$

Equation (A4) was found to be much easier to program into a code. The table below shows the magnitude of the overestimation of the actual ε_s^o when equation (A4) is used instead of equation (A3) (Table AI):

It could be seen from this table that the percent of the overestimation of ε_s^o gradually increases with the magnitude of the total strain.

The total true strain for any layer through the thickness of the tube is:

$$\varepsilon_s(z) = \varepsilon_s^o + z\kappa_s \tag{A5}$$

where κ_s is given by equation (12) when $K_1 = 0$.

Rotation of normal vector

We assume that the angle between the current normal vector $\hat{n}$ and S (arc length) to be α, and the angle between the current normal vector $\hat{n}$ and reference normal vector $\hat{N}$ to be β (Figures 2 and 4). Then we have:

$$\beta + \frac{\pi}{2} = \alpha; \quad \hat{n} \cdot \hat{A} = \cos\alpha = -\sin\beta \tag{A6}$$

Substituting equation (8) in Section 2 into equation (A6), we obtain:

$$\sin\beta = \frac{\mathrm{d}}{\lambda_1} = \frac{w_{,S} + K_1 u}{\lambda_1} = \frac{w_{,S} + K_1 u}{\sqrt{(1 + u_{,S} - K_1 w)^2 + (w_{,S} + K_1 u)^2}} \tag{A7}$$

For a straight line segment ($K_1 = 0$), by assuming that $(1 + u_{,S}) \approx 1$ and β is small, we get:

$$\sin\beta \approx \beta = \frac{w_{,S}}{\sqrt{1 + w_{,S}^2}} \tag{A8}$$

As shown in Figure 4, if the positive w direction is in the opposite direction of the normal vector to the mid-surface, $\hat{n}$, then $w_{,S}$ should be replaced with $-w_{,s}$.

ε_s^o from equation (A4)	${}^*\varepsilon_s^o$ from equation (A3)	$\delta = \varepsilon_s^o - {}^*\varepsilon_s^o$	$\delta/{}^*\varepsilon_s^o$ (percent)
0.001	0.0009995	$5 \times {}^{-7}$	0.05
0.01	0.009951	$4.9 \times {}^{-5}$	0.5
0.05	0.0488	$1.2 \times {}^{-3}$	2.5
0.10	0.0954	$4.6 \times {}^{-3}$	4.8
0.20	0.1832	$1.68 \times {}^{-2}$	9.2
0.25	0.2247	$2.53 \times {}^{-2}$	11.3
0.30	0.2649	$3.51 \times {}^{-2}$	13.3

Table AI.

The current principal centerline curvature

For a straight segment ($K_1 = 0$), the centerline curvature at the current configuration, k_x, will be obtained from equation (12) in Section 2:

$$\kappa_x = \frac{cd_{,S} - dc_{,S}}{\lambda_1^3} = \frac{(1 + u_{,S})w_{,SS} - w_{,S}u_{,SS}}{\lambda_1^3} \tag{A9}$$

By assuming that $1 + u_{,S} \approx 1$ and $u_{,SS} \approx 0$, equation (A9) could be approximated as:

$$\kappa_x \approx \frac{w_{,SS}}{\left(1 + w_{,S}^2\right)^{3/2}} \tag{A10}$$

Given the opposite direction of the normal vector to the mid-surface, $w_{,ss}$ in equation (A10) should be replaced with $-w_{,ss}$.

Corresponding author
Farhang Pourboghrat can be contacted at: pourbogh@egr.msu.edu